Translational Oncology
www.transonc.com

Volume 7 Number 2 April 2014 pp. 230–239 230

Monitoring of Tumor Response to Cisplatin Using Optical Spectroscopy

Jarich W. Spliethoff*, Daniel J. Evers*, Janneke E. Jaspers†, Benno H.W. Hendriks‡, Sven Rottenberg† and Theo J.M. Ruers*,§

*Department of Surgery, The Netherlands Cancer Institute, Amsterdam, The Netherlands; †Division of Molecular Biology, The Netherlands Cancer Institute, Amsterdam, The Netherlands; ‡Department of Minimally Invasive Healthcare, Philips Research, Eindhoven, The Netherlands; §MIRA Institute, Technical University Twente, Enschede, The Netherlands

Abstract

INTRODUCTION: Anatomic imaging alone is often inadequate for tuning systemic treatment for individual tumor response. Optically based techniques could potentially contribute to fast and objective response monitoring in personalized cancer therapy. In the present study, we evaluated the feasibility of dual-modality diffuse reflectance spectroscopy–autofluorescence spectroscopy (DRS-AFS) to monitor the effects of systemic treatment in a mouse model for hereditary breast cancer. *METHODS*: Brca1$^{-/-}$; p53$^{-/-}$ mammary tumors were grown in 36 mice, half of which were treated with a single dose of cisplatin. Changes in the tumor physiology and morphology were measured for a period of 1 week using dual-modality DRS-AFS. Liver and muscle tissues were also measured to distinguish tumor-specific alterations from systemic changes. Model-based analyses were used to derive different optical parameters like the scattering and absorption coefficients, as well as sources of intrinsic fluorescence. Histopathologic analysis was performed for cross-validation with trends in optically based parameters. *RESULTS*: Treated tumors showed a significant decrease in Mie-scattering slope and Mie-to-total scattering fraction and an increase in both fat volume fraction and tissue oxygenation after 2 days of follow-up. Additionally, significant tumor-specific changes in the fluorescence spectra were seen. These longitudinal trends were consistent with changes observed in the histopathologic analysis, such as vital tumor content and formation of fibrosis. *CONCLUSIONS*: This study demonstrates that dual-modality DRS-AFS provides quantitative functional information that corresponds well with the degree of pathologic response. DRS-AFS, in conjunction with other imaging modalities, could be used to optimize systemic cancer treatment on the basis of early individual tumor response.

Translational Oncology (2014) 7, 230–239

Introduction

Monitoring of the individual tumor response is crucial for optimizing systemic treatment in patients with cancer, particularly as treatments trend toward individualized patient care [1–4]. Therapy response assessment is generally performed by anatomic imaging using the standardized Response Evaluation Criteria In Solid Tumors criteria on the basis of changes in anatomic tumor size [5]. However, standard-of-care anatomic imaging modalities, such as computed tomography, are unable to objectively evaluate treatment response at the early stages of treatment. In addition, shrinkage of tumors can be minimal even when treatment is effective. This phenomenon is most obvious in certain tumor types, like sarcomas or gastrointestinal stromal tumors [6], as well as with new targeted drugs that lack direct intrinsic cytotoxic activity, such as bevacizumab [7].

A modality that is based on functional contrast rather than on anatomic features alone may improve response monitoring. An

Address to all correspondence to: Jarich W. Spliethoff, MSc, Department of Surgery, Plesmanlaan 121, 1066 CX, Amsterdam, The Netherlands. E-mail: j.spliethoff@nki.nl
Received 30 October 2013; Revised 7 December 2013; Accepted 2 January 2014

1936-5233/14 http://dx.doi.org/10.1016/j.tranon.2014.02.009

example of functional imaging is positron emission tomography (PET) using [^{18}F]fluorodeoxyglucose (^{18}F-FDG). Nowadays, ^{18}F-FDG PET has been used for early-response monitoring and outcome prediction, although the accuracy is still dependent on the tumor type and the treatment used [8–10].

In the last decade, optical sensing, by means of diffuse reflectance spectroscopy (DRS) and autofluorescence spectroscopy (AFS), has been used to improve the identification of cancerous lesions in various organs [11–21]. Both modalities enable tissue characterization by measuring the spectral response after the tissue is illuminated with a selected spectral band of light. Depending on the tissue composition and its structure, a specific "optical fingerprint" is acquired. This optical fingerprint represents specific quantitative morphologic, biochemical, and functional information from the probed tissue, making it a promising technique for the detection of chemotherapy-induced alterations.

Tromberg's group investigated the changes in optically measured biomarkers during chemotherapy in breast cancer using diffuse optical spectroscopy (DOS) [22–25]. DOS imaging using a handheld probe was used to scan the breasts of patients with locally advanced breast cancer before, during, and after chemotherapy. The results of these studies showed that optically derived tissue parameters strongly correlate with and, in some cases, predict pathologic response. A study by Falou et al. also suggested that responders and nonresponders could be differentiated with DOS [26]. Finally, the biomedical engineering group at Duke University (Durham, NC) showed that a combination of DRS and AFS can be applied to monitor drug concentrations and tumor physiology *in vivo* in a preclinical mouse model [27].

Studies thus far have mainly focused on the noninvasive application of optical sensing by hand-held optical transducers used to scan tissue surfaces. This approach has a clear advantage for breast tumors but may limit the applicability of optical sensing for deep-seeded tumors such as in the lung or kidney. Recently, we described an optical needle probe able to perform optical measurements in tumor tissue [21,28,29]. Optical measurements conducted through very fine needles (smaller than 27 G) open the potential to assess treatment response of (solid) tumors at deep-tissue sites [30]. The aim of this study was to investigate whether dual-modality DRS-AFS, incorporated in a small needle probe, was able to monitor the dynamics of tumor response after treatment with cisplatin using a preclinical mouse model for BRCA1-mutated breast cancer.

Materials and Methods

Animal Study Protocol

In this study, Brca1$^{-/-}$; p53$^{-/-}$ mammary tumors were generated in a mouse model for hereditary breast cancer previously described by Liu et al. [31]. These tumors have been demonstrated to be sensitive to cisplatin at a maximum tolerated dose (MTD) of 6 mg/kg i.v. [32].

Small fragments of tumor (1-2 mm in diameter) were orthotopically transplanted into the fourth right mammary fat pad of 36 female (FVB/N HanHSD WT) animals (The Netherlands Cancer Institute, Amsterdam, The Netherlands) (6-8 weeks of age) as described previously [32]. Starting 2 weeks after tumor grafting, the onset of tumor growth was checked at least three times per week. Tumor size was determined by caliper measurements (length and width in millimeters), and tumor volume (in cubic millimeters) was calculated using the following formula: 0.5 × length × width^2.

Once the tumor volume reached 400 to 800 mm^3, the animals were separated into control and treatment groups. Animals in the treatment group (N = 18) received cisplatin (1 mg/ml in saline/mannitol) at a dose of 6 mg/kg (MTD) in a single i.v. injection into the tail vein. Animals in the control group (N = 18) received an equivalent amount of saline.

DRS and AFS tumor measurements were performed *in vivo* after inserting the spectroscopy needle percutaneously (through the skin) into the tumors. Baseline measurements were performed on day 0, immediately after treatment/placebo administration, and then on days 1, 2, 4, and 7 afterwards. These time points were selected from a previous pilot study. To evaluate whether eventual changes in the optical profile were systemic or tumor specific, eight animals from each group were randomly chosen for additional *in vivo* measurements in liver and muscle tissues on days 2, 4, and 7.

After each session of optical measurements, three to five animals from each group were killed to obtain tumor tissue for histopathologic evaluation. Tumor samples were dissected into three parts: these were snap frozen in liquid nitrogen, fixed in 4% formalin, or fixed in acetic acid–formalin ethanol saline.

The tumor model used is known to be very sensitive to the MTD of cisplatin, whereas nontreated tumors grow rapidly. This could result in control animals being removed from the experiment on the basis of humane end points (tumor volume >1500 mm^3) or in a minimal amount of measurable tumor tissue in the treated animals before the end of the experiment. Therefore, animals with slightly higher tumor volumes were included in the treatment group. Throughout the course of the experiment, starting 3 weeks before the tumor grafting, the animals were given a purified diet to eliminate autofluorescence from chlorophyll [33]. During the optical spectroscopy measurements, the animals were deeply anesthetized using 1.5% isoflurane mixed with oxygen. All animal procedures were approved by the Animal Ethics Committee of the Netherlands Cancer Institute.

Optical Spectroscopy Using a Miniaturized Optical Probe

DRS and AFS measurements were performed using a portable spectroscopic system, which consists of two light sources and two spectrometers (Figure 1). For the DRS measurements, a Tungsten halogen broadband light source (360-2500 nm) with an embedded shutter was used. For AFS, the system was equipped with a semiconductor laser (λ = 377 nm) to induce autofluorescence. One spectrometer was used to resolve light in the visible wavelength range, i.e., 400 until 1100 nm (DU420A-BRDD; Andor Technology, Belfast, Northern Ireland), the other to resolve near-infrared light from 900 to 1700 nm (DU492A-1.7; Andor Technology). The spectrometers were controlled by a custom-made LabVIEW software user interface (National Instruments, Austin, TX) to acquire and save the data. The calibration procedure has been described elaborately by Nachabe et al. [34].

A custom fiber-optic needle that can probe tissue at the needle tip was developed. The needle consisted of a 21-G (0.82 mm) outer cannula and a 22-G adjustable stylet (Figure 1*B*), containing four identical fibers with a core diameter of 100 μm. To minimize tissue damage, the optical fibers were retracted during needle insertion. The optical fibers were protruded after positioning the needle at the right position to establish optimal tissue contact. Two fibers were connected to the broadband light source and laser, whereas the two other fibers were connected to the spectrometers to capture diffusely

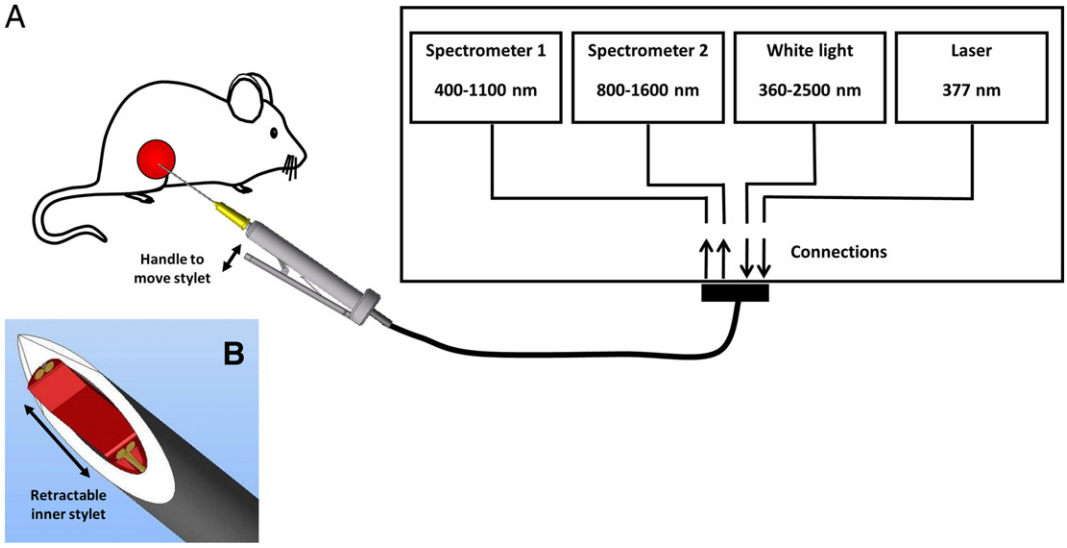

Figure 1. Schematic overview of the combined DRS and AFS optical setup. The system measures diffuse reflectance (400-1600 nm) and intrinsic fluorescence (400-800 nm) of tissue through the use of a miniaturized 21-G needle with a retractable inner fiber-optic stylet.

scattered light and fluorescence from the tissue. Two different source-detector separations (SDSs) were used (1.5 and 0.15 mm). The spectra acquired with the 1.5-mm SDS were used for the DRS data analyses, whereas the DRS spectra measured with the 0.15-mm SDS were used to correct for absorption and scattering in the fluorescence spectra.

Diffuse Reflectance Spectral Analysis

Three to five DRS spectra were collected from each animal on each measurement day, consecutively. To interpret the acquired DRS spectra, a widely accepted analytical model, introduced by Farrell et al. [35], was used to estimate the various DRS absorption and scattering coefficients. The absorption coefficients represent the concentration of physiologically relevant absorbers in the tissue, such as hemoglobin, water, and fat, as well as functional parameters like tissue oxygenation. The main scattering parameters are the reduced scattering coefficient (at 800 nm), the reduced scattering slope of the Mie scatterer (Mie-scattering slope), and the Mie-to-total scattering fraction. The Mie-scattering slope is related to the average particle size [36]. In the Mie-to-total scattering fraction, the total scattering of tissue is assumed to be composed of Mie and Rayleigh scattering. In tissue, Mie scattering represents scattering caused by biologic cells and cellular components, whereas Rayleigh scattering is elastic scattering of light by particles that are much smaller than the wavelength of light (e.g., macromolecular aggregates such as collagen fibrils). The validation of the DRS analytic method has been described previously by our group [34,37].

Intrinsic Fluorescence Modeling and Quantification

Intrinsic fluorescence from the tissue was calculated by correcting the acquired fluorescence spectra for absorption and scattering using the short SDS DRS spectra. For the latter, a modified photon migration method [38] was used on the basis of the work by Müller et al. [39] and Zhang et al. [40]. The corrected spectra were fitted using the fluorescence spectra (excitation at 377 nm) of endogenous tissue fluorophores [collagen, elastin, nicotinamide adenine dinucleotide (NADH), and flavin adenine dinucleotid (FAD)] as *a priori* knowledge. The optical oxidation-reduction (redox) ratio, which is linked to the metabolic state of the tissue, was defined as NADH/(NADH +FAD) [41,42]. Because collagen and elastin have almost identical fluorescence spectra, estimated amounts of collagen and elastin were combined as collagen + elastin.

In case the tissue contained diagnostic levels of endogenous fluorophores other than the ones included in the standard fit model, the area underneath the fitted curve (known fluorophores) was subtracted from the total area under the original curve (measured fluorescence).

Histopathologic Analyses

Samples were stained with both standard hematoxylin and eosin (Merck, Darmstadt, Germany) (HE) and Masson trichrome (MT) (Sigma-Aldrich, St. Louis, MO) dyes. The HE-stained sections were used to quantify vital, necrotic, and fibrotic tissue fractions. The necrotic and fibrotic fractions were calculated as a percentage of the overall tissue area across each section. For this purpose, at least 10 different fields were investigated at a 400× magnification.

Immunohistochemical analysis of tumors was performed using anti-γH2AX [rabbit polyclonal; Cell Signaling Technology (Beverly, MA), No. 2577, 1:50 in 1% BSA diluted in phosphate saline buffer], anti–cleaved caspase 3 (CC3) [rabbit polyclonal; Cell Signaling Technology, No. 9661, 1:100 in 1% phosphate-buffered saline with bovine serum albumin], and anti–Ki-67 probes (Dako (Glostrup, Denmark); 1:100). For evaluation of the amount of lipids, frozen sections were mounted on glass slides and stained with Oil Red O (Sigma-Aldrich, St. Louis, MO). All histopathology was evaluated by an experienced pathologist in a blinded study setting. The pathology findings were used to cross-validate the longitudinal changes in the optical end-points.

Two-Photon Excitation Microscopy

Intrinsic fluorescence in tumor was imaged using a two-photon confocal microscopy setup. These experiments were carried out to relate the differences in fluorescence spectra obtained with AFS to specific structures in the tissue slices. Snap-frozen tumor pieces were sliced in thick sections (25 μm), kept unstained and unfixed, and

mounted onto glass microscope slides. The two-photon excitation source was a Ti:Sapphire laser (Tsunami, Spectra Physics, Santa Clara, CA) tuned to 790 nm. The excitation light (equivalent to a single-photon excitation wavelength of 395 nm) was delivered to, and the emitted light was collected from the sample through a Leica Confocal microscope [with a Leica (Mannheim, Germany) HCX IRAPO 25× water immersion objective with an NA of 0.95] coupled to a Leica TCS SP5 tandem scan head operating at 500 lines per second. A photomultiplier served as the detector. For each tumor sample, fluorescence images were obtained in the wavelength ranges of 400 to 500 nm, 500 to 600 nm, and 600 to 700 nm. This was done to compare the relative intensity of fluorescence at these spectral ranges between treated and control animals.

Statistical Analysis

To examine the trends in optical parameters over time, a linear regression model was performed in MATLAB 7.13 (MathWorks Inc, Natick, MA). The fixed-effects terms in the models were treatment (controls *vs* cisplatin), time (day), and their interactions. A slope and intercept were fit for the data of both the treated and control groups using maximum likelihood estimation. For the significance of fixed effects, a likelihood ratio test was statistically compared to a χ^2 distribution with 1 *df* (for one coefficient being eliminated). For all tests, statistical significance was set at $P < .05$.

Results

Longitudinal Trends in DRS Parameters and Tumor Volume

DRS parameter quantification was performed as part of the model-based data analysis using a total of 712 DRS spectra. The longitudinal changes for the average tumor volume and various DRS parameters over time are shown in Figure 2. In the control animals, the tumor volume increased during the entire follow-up period, whereas the tumors of the cisplatin-treated animals started to shrink 2 days after treatment. For the DRS parameters, the trends during follow-up were significantly different between the treated and the control groups for the Mie-scattering slope ($P < .0001$), Mie-to-total scattering fraction ($P < .001$), tissue oxygenation ($P = .035$), and fat volume fraction ($P < .0001$).

Longitudinal Trends in AFS Parameters

The fluorescence spectra and corresponding model fits for two representative animals (one treated and one control animal) on days 0, 2, 4, and 7 are shown in Figure 3. In the tumor of the treated animal, an increasing deviation between the measurements and the fitted curves was observed from day 2 onwards, between 500 and 800 nm. This indicates that fluorophores other than the ones included in the standard fit model (collagen, elastin, NADH, and FAD) were measured. This additional fluorescence activity (from now on called fluorescence residual) was seen in all the treated tumors at days 4 and 7.

The longitudinal kinetics for each model-fitted AFS parameter and the calculated fluorescence residual across all treated and control animals are shown in Figure 4. The plotted linear trend for the fluorescence residual in tumor was significantly different between the treated and the control groups ($P = .018$). No significant trends were observed for the total fluorescence intensity, collagen + elastin, and the optical redox ratio.

Figure 5 shows the longitudinal changes of the fluorescence residual in tumor, liver, and muscle across all animals from both groups. The additional fluorescence is not present in muscle and liver tissues, indicating a tumor-specific effect.

Two-Photon Confocal Microscopy

In an attempt to better understand the origin of the additional autofluorescent emission (mainly above 600 nm) seen in the treated animals, two-photon confocal fluorescence microscopy images recorded in a spectral range of 600 to 700 nm were compared with adjacent tissue sections that were stained with HE (Figure 6). The

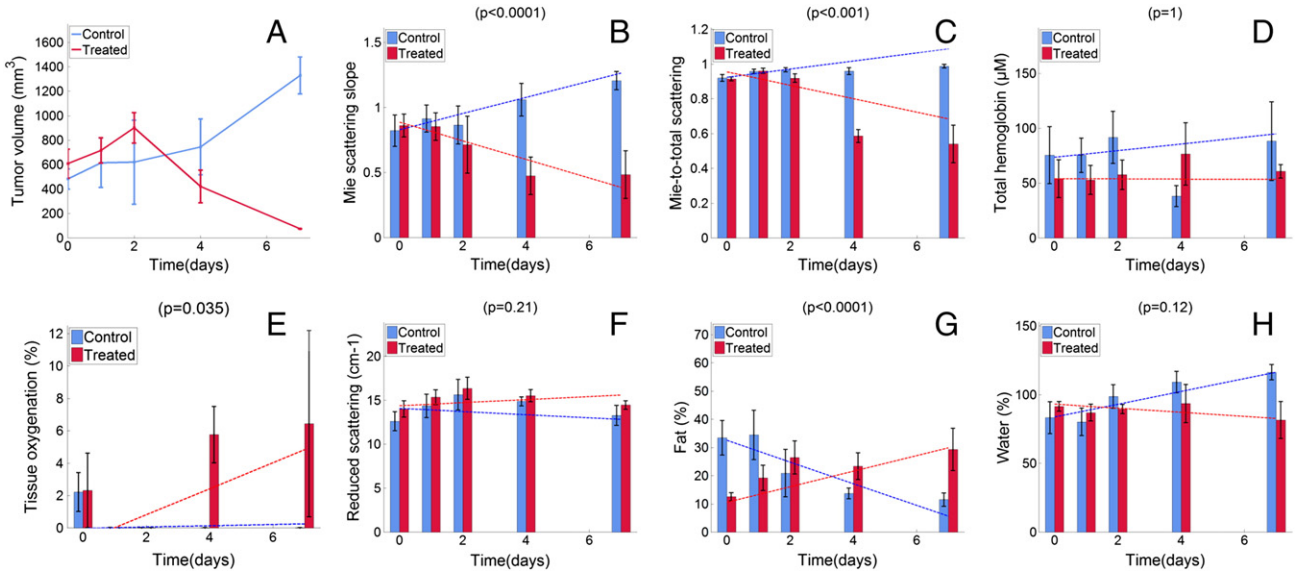

Figure 2. Longitudinal changes in tumor volume and DRS parameters measured for both groups across time: tumor volume (A), Mie-scattering slope (B), Mie-to-total scattering fraction (C), total hemoglobin (D), tissue oxygenation (E), reduced scattering (F), fat volume fraction (G), and water volume fraction (H). The bars represent the means for each parameter computed across all available animals, at each particular time point, for both the treated (red) and control (blue) groups. The dashed lines represent the corresponding regression lines. *P* values are shown at the top of each plot.

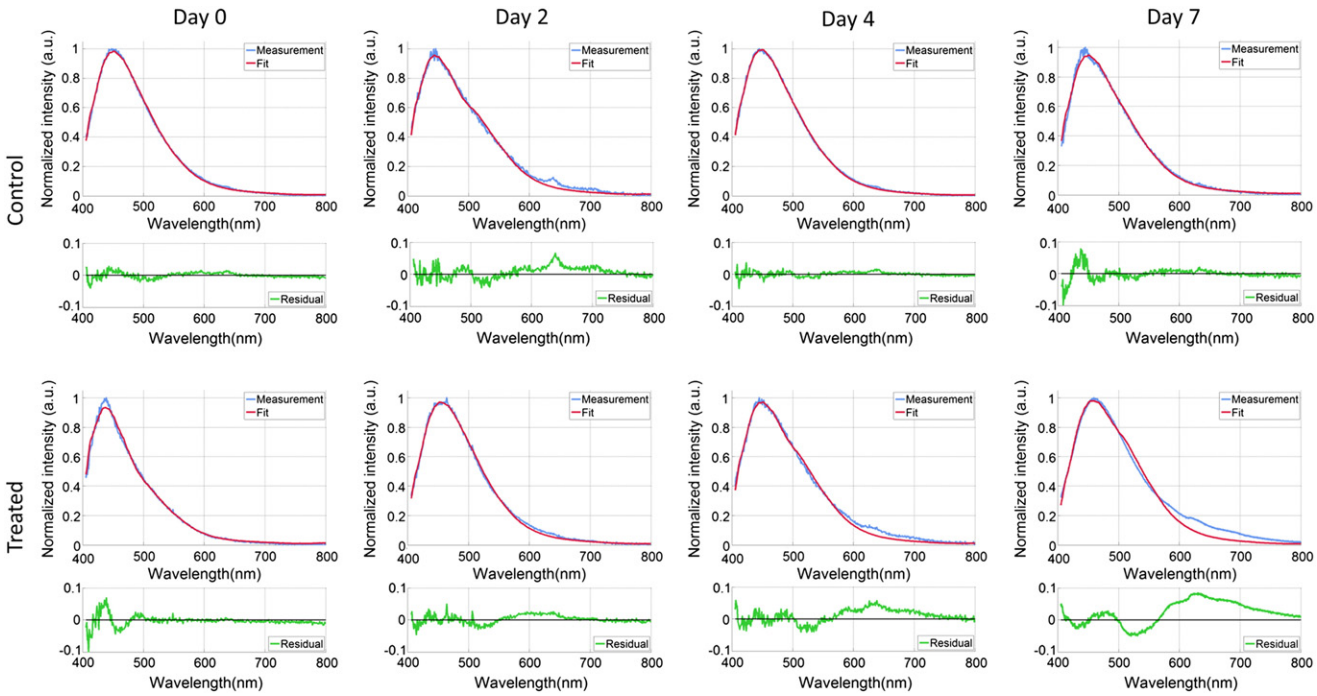

Figure 3. Autofluorescence spectra for a representative animal in the control group and the treated group during 1 week of follow-up. The blue lines are the fluorescence measurements, whereas the red lines are the results of the model-based fitting procedure. The green lines illustrate the residual due to the presence of additional fluorescence, which is specifically seen in the treated animals after 2 days.

samples were collected after 1 week of follow-up, i.e., when the differences seen in AFS signals were maximal. In the treated tumor samples, numerous fluorescent foci were present. These foci correlated with cellular structures rather than with collagen deposits or necrotic areas. It remains to be determined whether this specific fluorescence originated from stromal or tumor cells. For the two-photon images recorded in the spectral ranges 400 to 500 nm and 500 to 600 nm, no considerable differences were seen when comparing both groups.

Evaluation of Histology and Histochemical Biomarkers

The evaluation of pathologic response of tumors to cisplatin using various histologic dyes and immunohistochemical biomarkers is illustrated in Figure 7. A strong increase in nuclear DNA damage was seen 24 hours after cisplatin administration using γ-H2AX as a marker. From day 2 onwards, a significant decrease in the proliferation marker Ki-67 and an increase in apoptosis-related cell death (CC3 marker) were observed. Analysis of MT-stained slides showed increased amounts of fibrotic tissue 4 to 7 days after treatment that corresponded to the HE images. An increase in lipids (Oil Red O) was seen over time.

In Figure 8, *A* and *B*, fractions of vital, necrotic, and fibrotic tumor tissues for both groups are shown as quantified on the HE-stained tissue slides. These data indicate that the pathologic response to cisplatin in this tumor model corresponds with the replacement of viable tumor tissue by fibrosis, without a considerable increase in necrosis. The longitudinal changes in these histopathologic end points were compared against changes in prominent optical parameters as shown in Figure 8, *C* and *D*. In the treated group, a major shift in both histology and optical end points was seen, whereas minimal changes were observed across all of these parameters in the control group.

Discussion

In this study, a combination of DRS and AFS was used to investigate cisplatin-induced changes in tumor physiology and morphology

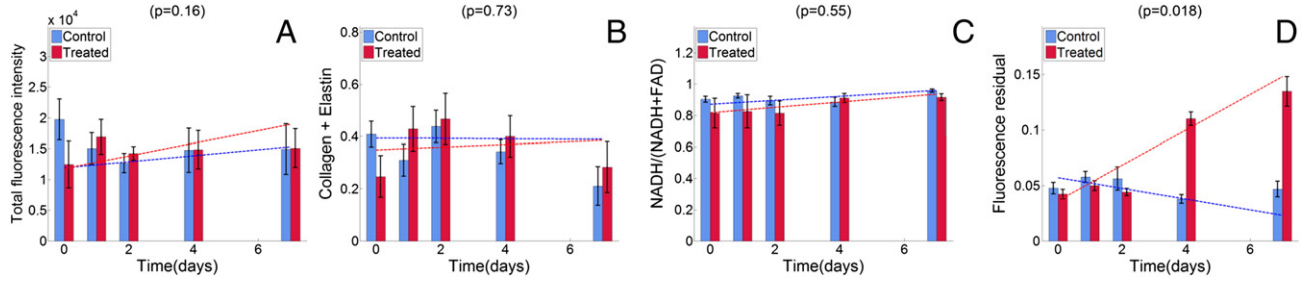

Figure 4. Longitudinal trends in AFS parameters measured for both groups across time: total fluorescence intensity (A), collagen + elastin (B), optical redox ratio (C), and fluorescence residual (D). The bars represent the means for each parameter computed across all available animals, at each particular time point, for both the treated (red) and control (blue) groups. The error bars are SEs. The dashed lines represent the corresponding regression lines. *P* values are shown at the top of each.

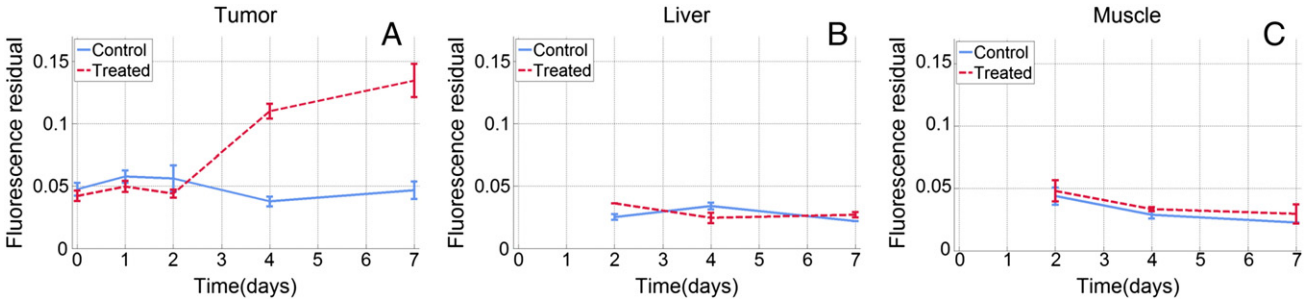

Figure 5. Course of fluorescence residual in tumor (A), liver tissue (B), and muscle tissue (C) over time. The data of muscle and liver tissues shown here were obtained from 16 (8 per group) of the animals that were killed at day 2, 4, or 7, whereas A represents the full cohort. The error bars are SEs.

across a period of 1 week in a mouse model for hereditary breast cancer. The changes in optical end points were compared against the degree of pathologic response. The results showed that various DRS and AFS parameters in the treated animals significantly changed throughout the course of treatment relative to the untreated animals. These parameters were the Mie-scattering slope ($P < .0001$), Mie-to-total scattering fraction ($P < .001$), tissue oxygenation ($P = .035$), fat volume fraction ($P < .0001$), and fluorescence residual ($P < .018$). Furthermore, the observed changes appeared to be proportional to the degree of vital tumor tissue and the formation of fibrosis.

Optical scattering characteristics are dependent on the size and density of cell nuclei and organelles as well as on the composition of the extracellular matrix (e.g., macromolecular aggregates and collagen fibers). In the histopathologic evaluation, considerable alterations in the extracellular matrix (formation of fibrosis) and in the size and the density of (sub) cellular structures were observed in the tumors of the treated

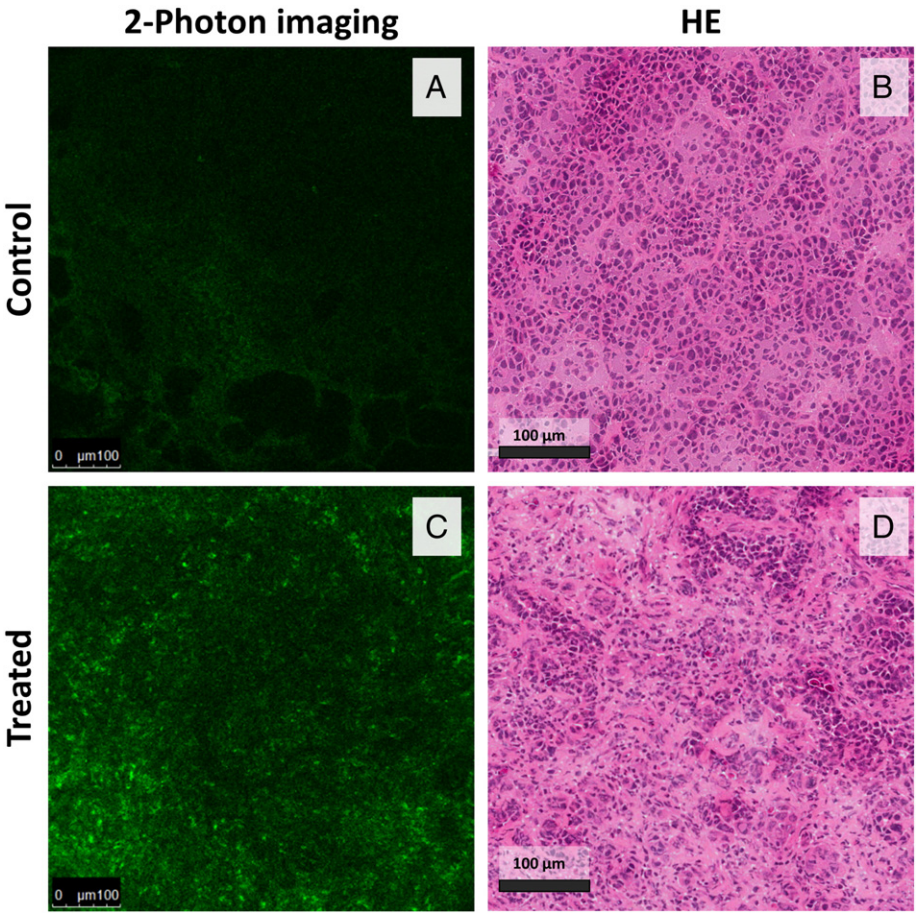

Figure 6. Two-photon confocal microscopy images (600-700 nm) of tumor sections of a representative control (A) and treated animal (C). Effective excitation was at 395 nm, and the intensity scale is the same in both of the two-photon images. The samples were collected after 1 week of follow-up, i.e., when the differences seen in AFS signals were maximal. In the treated tumor samples, numerous fluorescent foci were present within the cells. B and D show corresponding HE images.

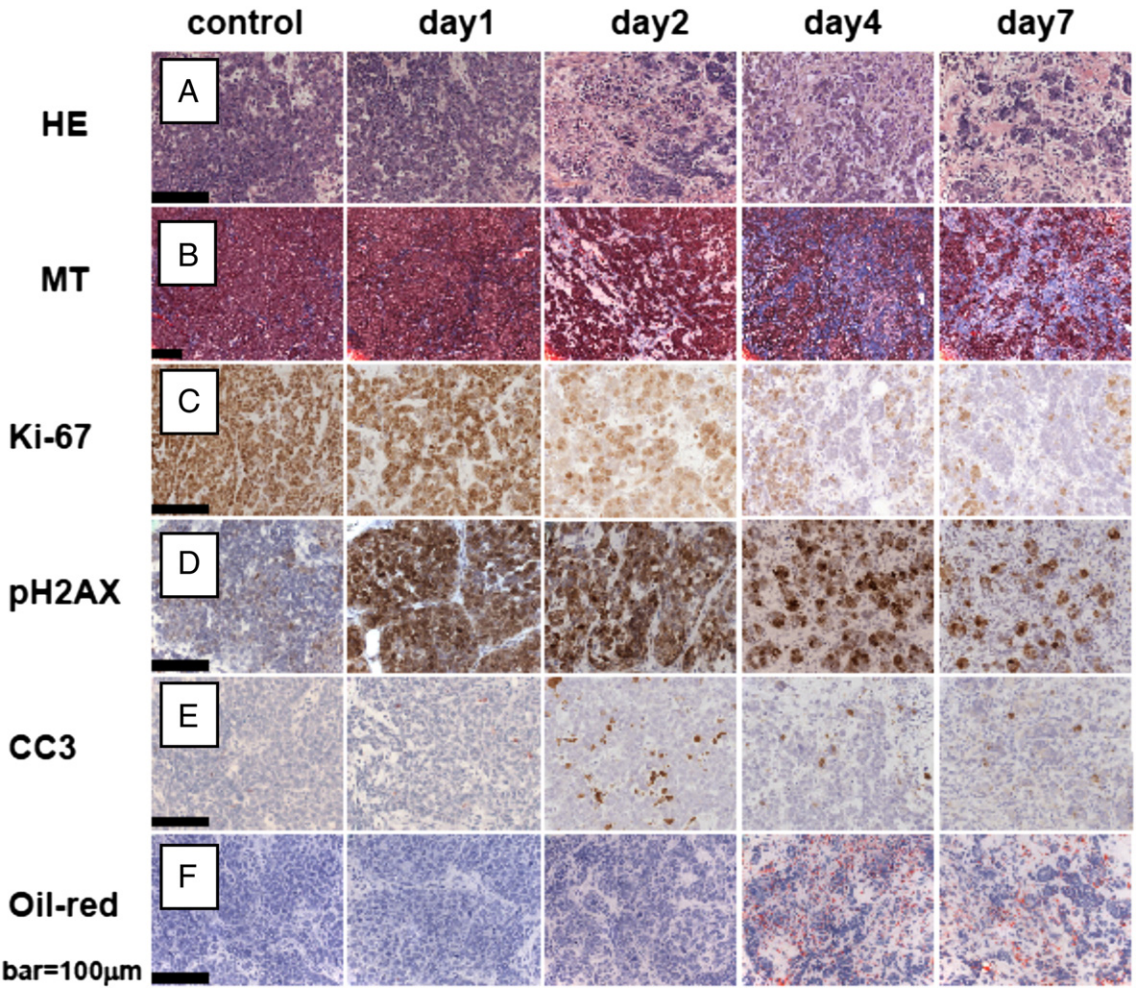

Figure 7. Tumor pathologic response to an MTD cisplatin. Scale bar, 100 μm. HE- (A) and MT- (B) stained tumor sections show replacement of viable tumor tissue by fibrosis, especially after day 2 onwards. The γ-H2AX (C), Ki-67 (D), and anti-CC3 (E) markers showed a strong increase in DNA damage, a decrease in proliferation, and an increase in apoptosis-related cell death, respectively. An increase in the amount of lipids (Oil Red O stain) was seen across time.

animals. These morphologic and structural changes may lead to changes in tissue-scattering properties that in turn may translate into changes in the Mie-scattering slope and Mie-to-total scattering fraction. Although significant fibrosis and cellular disintegration after treatment with cisplatin may explain these specific changes, further research is needed to provide a better understanding of these relationships.

Tumor tissue oxygenation values of untreated animals remained hypoxic over time, whereas tumors of treated animals became progressively more oxygenated. This is consistent with previously reported results where improved oxygenation of tumor tissue was observed due to tumor regression and altered metabolism after treatment with doxorubicin [27,43,44]. For example, Vishwanath et al. performed DRS using a surface probe and showed that mammary-tumor tissue oxygenation in treated mice increased after doxorubicin administration relative to the untreated controls.

A particularly interesting finding was the additional fluorescence observed in the treated group. On the basis of two-photon imaging, the extra fluorescence was specifically found in the cellular components of tumor tissue treated with cisplatin. Fluorescence was tumor specific and not observed in liver or muscle tissue of the treated animals. Earlier research has shown that some cancers accumulate diagnostic levels of endogenous protoporphyrin IX and other metabolic products of porphyrin as a result of tumor-specific metabolic alterations [45,46]. Quantification of porphyrins using standard fit procedures is challenging, because the exact wavelength of the fluorescence bands of porphyrins strongly depend on the environment (e.g., pH) where it is measured [45,46]. Whether porphyrin fluorescence is primarily associated with certain tumor types or with response to systemic therapy is unknown. The exact basis of the additional autofluorescence emission observed in this study will be investigated in future studies.

The AFS spectra were fitted using the intrinsic fluorescence spectra of collagen, elastin, NADH, and FAD as *a priori* knowledge. No considerable change over time was observed in these parameters. This may be due to the presence of significant amounts of unknown fluorescence that was not taken into account in the AFS curve fitting procedure and hence may have influenced quantification of minor effects of the other fluorophores such as collagen, elastin, NADH, and FAD.

The use of a broad spectral range in combination with a model-based analysis allows proper estimation of most individual DRS parameters. Some caution is advised concerning the total hemoglobin contents within this study. Although a thin 21-G optical needle (0.72 mm) was used, minor bleeding at the tip of the needle may have

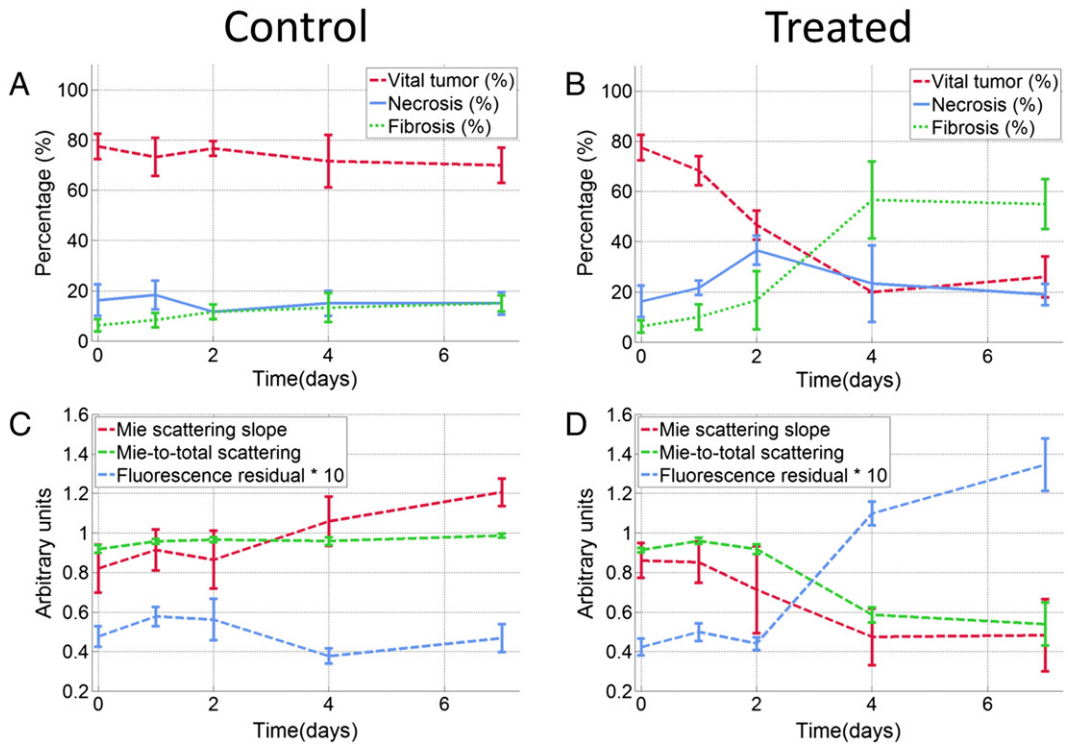

Figure 8. Comparison of histology and optical spectroscopy end points. The upper two figures show the temporal changes in mean fractions of vital tumor tissue, necrosis, and fibrosis for the control (A) and treated (B) groups, as assessed by histologic staining using HE. The lower two figures (C and D) show temporal changes in the Mie-scattering slope, the Mie-to-total scattering fraction, and the fluorescence residual for both groups. Error bars indicate SE.

caused high values for average total hemoglobin content. However, in a previous clinical study by Brown et al. [47] a 14-G coaxial cannula combined with a fiber-optic needle was successfully used to measure tissue optical properties in human breast tissue during surgery. This indicates that small bleedings are not necessarily a problem when optical spectroscopy technology is applied *in vivo*. It also indicates the feasibility, within a clinical setting, of monitoring changes in perfusion and blood content of tumors by using a needle-based fiber-optic tool. Both parameters may be of specific interest for evaluation of tumor responses to antiangiogenic drugs.

Earlier research suggests that cancer cells show specific alterations in different aspects of lipid metabolism. For example, the high proliferation of cancer cells requires large amounts of lipids as building blocks for biologic membranes [48], whereas apoptosis-related cell death is associated with an accumulation of cellular lipids [49]. Our setup is able to measure in the infrared wavelength range up to 1600 nm where fat and water absorption bands exist. This enables reliable estimation of these substances [34]. In this study, histopathologic analysis using Oil Red O showed an increase in the amount of lipids in tumor sections for the treated animals. This is consistent with the increase in apoptosis-related cell death seen in the anti-CC3 images and the clear increase in fat volume fraction ($P < .0001$) measured with DRS for the same animals. Regarding the control group, the high offset of fat percentage at day 0 and the decrease in the average fat volume fraction during follow-up may be explained by the lower average "starting" tumor volume in the control animals (compared to the treated animals), as well as the subsequent progressive growth of these tumors and the associated decrease in lipid content.

In the current study, we used a tumor model that is known to be very sensitive to the MTD of cisplatin. Further studies in animal models with drug-resistant tumors are needed to explore the differences in optical parameters in these settings. Moreover, it is likely that the changes in tumor tissue vary on the basis of the specific treatment given. To provide a more complete understanding of the relationship between optical spectroscopy parameters and pathologic response, the effect of other drugs on spectroscopy parameters needs to be investigated further.

Conventional anatomic imaging alone lacks the sensitivity for early-response monitoring or assessing the effect of new targeted therapies that do not necessarily result in a change in tumor size. For these purposes, functional information, such as that obtained by ^{18}F-FDG PET [7–9] and contrast-enhanced magnetic resonance imaging [50] is more suitable. Optical spectroscopy is a relatively new functional imaging technique that may contribute to fast-response evaluation and timely shifting of systemic treatment. This could be of great clinical benefit, even when it requires (minimal) invasive optical spectroscopy measurements in the tumor. In a time of personalized medicine, repeated tumor core biopsy is increasingly used during the course of treatment to generate a genetic or epigenetic profile allowing selection of the best possible treatment. Repeated biopsies may, however, be confounded by intratumor heterogeneity [51]. By performing optical spectroscopy along the needle path, an "optical tumor profile" can be recorded covering a relatively large volume of tumor tissue. For example, Nachabe et al. [52] showed that optical spectroscopy measurements at the tip of a needle allowed real-time tissue characterization during percutaneous interventions. As such, optical spectroscopy offers the potential to measure real time alterations in the optical profile during systemic treatment. In this way, it may help to personalize cancer treatments and may improve cost effectiveness of systemic treatment in cancer.

Conclusions

In summary, this study shows that dual-modality DRS–AFS provides quantitative functional information that corresponds well with the degree of pathologic response of systemic treatment. This could be of considerable value for the monitoring and prediction of cancer therapy efficacy on the basis of individual patient response. Further studies including resistant tumor models and various therapeutic drugs are needed to verify the initial findings of this work.

Acknowledgments

The authors thank the members of the Netherlands Cancer Institute animal facility and Philips Research project members for their support. In particular, the authors thank Walter Bierhoff for the probe development, Gert 't Hooft for assistance with the two-photon fluorescence imaging, and Ariana Kersbergen and Wendy Sol for their help with the animal experiments.

References

[1] Lordick F, Ruers T, Aust DE, Collette L, Downey RJ, El Hajjam M, Flamen P, Haustermans K, Ilson D, and Julié C, et al (2008). European Organisation of Research and Treatment of Cancer (EORTC) Gastrointestinal Group: Workshop on the role of metabolic imaging in the neoadjuvant treatment of gastrointestinal cancer. *Eur J Cancer* **44**, 1807–1819.

[2] Ollivier L, Balu-Maestro C, and Leclère J (2005). Imaging in evaluation of response to neoadjuvant breast cancer treatment. *Cancer Imaging* **5**, 27–31.

[3] Pons F, Duch J, and Fuster D (2009). Breast cancer therapy: the role of PET-CT in decision making. *Q J Nucl Med Mol Imaging* **53**, 210–223.

[4] Lim JS, Yun MJ, Kim MJ, Hyung WJ, Park MS, Choi JY, Kim TS, Lee JD, Noh SH, and Kim KW (2006). CT and PET in stomach cancer: preoperative staging and monitoring of response to therapy. *Radiographics* **26**, 143–156.

[5] Eisenhauer EA, Therasse P, Bogaerts J, Schwartz LH, Sargent D, Ford R, Dancey J, Arbuck S, Gwyther S, and Mooney M, et al (2009). New response evaluation criteria in solid tumours: revised RECIST guideline (version 1.1). *Eur J Cancer* **45**, 228–247.

[6] Wahl RL, Jacene H, Kasamon Y, and Lodge MA (2009). From RECIST to PERCIST: Evolving considerations for PET response criteria in solid tumors. *Eur J Cancer* **50**, 122S–150S.

[7] Chung WS, Park MS, Shin SJ, Baek SE, Kim YE, Choi JY, and Kim MJ (2012). Response evaluation in patients with colorectal liver metastases: RECIST version 1.1 *versus* modified CT criteria. *Am J Roentgenol* **199**, 809–815.

[8] Byström P, Berglund A, Garske U, Jacobsson H, Sundin A, Nygren P, Frödin JE, and Glimelius B (2009). Early prediction of response to first-line chemotherapy by sequential [^{18}F]-2-fluoro-2-deoxy-D-glucose positron emission tomography in patients with advanced colorectal cancer. *Ann Oncol* **20**, 1057–1061.

[9] de Geus-Oei LF, van Laarhoven HW, Visser EP, Hermsen R, van Hoorn BA, Kamm YJ, Krabbe PF, Corstens FH, Punt CJ, and Oyen WJ (2008). Chemotherapy response evaluation with FDG-PET in patients with colorectal cancer. *Ann Oncol* **19**, 348–352.

[10] Hendlisz A, Golfinopoulos V, Garcia C, Covas A, Emonts P, Ameye L, Paesmans M, Deleporte A, Machiels G, and Toussaint E, et al (2012). Serial FDG–PET/CT for early outcome prediction in patients with metastatic colorectal cancer undergoing chemotherapy. *Ann Oncol* **23**, 1687–1693.

[11] Mirabal YN, Chang SK, Atkinson EN, Malpica A, Follen M, and Richards-Kortum R (2002). Reflectance spectroscopy for *in vivo* detection of cervical precancer. *J Biomed Opt* **7**, 587–594.

[12] Nordstrom RJ, Burke L, Niloff JM, and Myrtle JF (2001). Identification of cervical intraepithelial neoplasia (CIN) using UV-excited fluorescence and diffuse-reflectance tissue spectroscopy. *Lasers Surg Med* **29**, 118–127.

[13] Georgakoudi I, Sheets EE, Muller MG, Backman V, Crum CP, Badizadegan K, Dasari RR, and Feld MS (2002). Trimodal spectroscopy for the detection and characterization of cervical precancers *in vivo*. *Am J Obstet Gynecol* **186**, 374–382.

[14] Breslin TM, Xu F, Palmer GM, Zhu C, Gilchrist KW, and Ramanujam N (2004). Autofluorescence and diffuse reflectance properties of malignant and benign breast tissues. *Ann Surg Oncol* **11**, 65–70.

[15] Utzinger U, Brewer M, Silva E, Gershenson D, Blast Jr RC, Follen M, and Richards-Kortum R (2001). Reflectance spectroscopy for *in vivo* characterization of ovarian tissue. *Lasers Surg Med* **28**, 56–66.

[16] Wallace MB, Perelman LT, Backman V, Crawford JM, Fitzmaurice M, Seiler M, Badizadegan K, Shields SJ, Itzkan I, and Dasari RR, et al (2000). Endoscopic detection of dysplasia in patients with Barrett's esophagus using light-scattering spectroscopy. *Gastroenterology* **119**, 677–682.

[17] Müller MG, Valdez TA, Georgakoudi I, Backman V, Fuentes C, Kabani S, Laver N, Wang Z, Boone CW, and Dasari RR, et al (2003). Spectroscopic detection and evaluation of morphologic and biochemical changes in early human oral carcinoma. *Cancer* **97**, 1681–1692.

[18] Keller MD, Majumder SK, Kelley MC, Meszoely IM, Boulos FI, Olivares GM, and Mahadevan-Jansen A (2010). Autofluorescence and diffuse reflectance spectroscopy and spectral imaging for breast surgical margin analysis. *Lasers Surg Med* **42**, 15–23.

[19] Volynskaya Z, Haka AS, Bechtel KL, Fitzmaurice M, Shenk R, Wang N, Nazemi J, Dasari RR, and Feld MS (2008). Diagnosing breast cancer using diffuse reflectance spectroscopy and intrinsic fluorescence spectroscopy. *J Biomed Opt* **13**, 024012.

[20] Bard MP, Amelink A, Skurichina M, Noordhoek Hegt V, Duin RP, Sterenborg HJ, Hoogsteden HC, and Aerts JG (2006). Optical spectroscopy for the classification of malignant lesions of the bronchial tree. *Chest* **129**, 995–1001.

[21] Spliethoff JW, Evers DJ, Klomp HM, van Sandick JW, Wouters MW, Nachabe R, Lucassen GW, Hendriks BH, Wesseling J, and Ruers TJ (2013). Improved identification of peripheral lung tumors by using diffuse reflectance and fluorescence spectroscopy. *Lung Cancer* **80**, 165–171.

[22] O'Sullivan TD, Leproux A, Chen JH, Bahri S, Matlock A, Roblyer D, McLaren CE, Chen WP, Cerussi AE, and Su MY, et al (2013). Optical imaging correlates with magnetic resonance imaging breast density and reveals composition changes during neoadjuvant chemotherapy. *Breast Cancer Res* **15**, R14.

[23] Ueda S, Roblyer D, Cerussi A, Durkin A, Leproux A, Santoro Y, Xu S, O'Sullivan TD, Hsiang D, and Mehta R, et al (2012). Baseline tumor oxygen saturation correlates with a pathologic complete response in breast cancer patients undergoing neoadjuvant chemotherapy. *Cancer Res* **72**, 4318–4328.

[24] Cerussi A, Hsiang D, Shah N, Mehta R, Durkin A, Butler J, and Tromberg BJ (2007). Predicting response to breast cancer neoadjuvant chemotherapy using diffuse optical spectroscopy. *Proc Natl Acad Sci U S A* **104**, 4014–4019.

[25] Cerussi AE, Tanamai VW, Mehta RS, Hsiang D, Butler J, and Tromberg BJ (2010). Frequent optical imaging during breast cancer neoadjuvant chemotherapy reveals dynamic tumor physiology in an individual patient. *Acad Radiol* **17**, 1031–1039.

[26] Falou O, Soliman H, Sadeghi-Naini A, Chemotherapy N, Lemon-wong S, Zubovits J, Spayne J, Dent R, Trudeau M, and Boileau JF, et al (2012). Diffuse Optical Spectroscopy Evaluation of Treatment Response in Women with Locally Advanced Breast Cancer Receiving Neoadjuvant Chemotherapy. *Transl Oncol* **5**, 238–246.

[27] Vishwanath K, Yuan H, Barry WT, Dewhirst MW, and Ramanujam N (2009). Using optical spectroscopy to longitudinally monitor physiological changes within solid tumors. *Neoplasia* **11**, 889–900.

[28] Nachabé R, Evers DJ, Hendriks BH, Lucassen GW, van der Voort M, Rutgers EJ, Peeters MJ, Van der Hage JA, Oldenburg HS, and Wesseling J, et al (2011). Diagnosis of breast cancer using diffuse optical spectroscopy from 500 to 1600 nm: comparison of classification methods. *J Biomed Opt* **16**, 087010.

[29] Evers DJ, Nachabé R, Hompes D, van Coevorden F, Lucassen GW, Hendriks BH, van Velthuysen ML, Wesseling J, and Ruers TJ (2013). Optical sensing for tumor detection in the liver. *Eur J Surg Oncol* **39**, 68–75.

[30] Hsu CP, Razavi MK, So SK, Parachikov IH, and Benaron DA (2005). Liver tumor gross margin identification and ablation monitoring during liver radiofrequency treatment. *J Vasc Interv Radiol* **16**, 1473–1478.

[31] Liu X, Holstege H, van der Gulden H, Treur-Mulder M, Zevenhoven J, Velds A, Kerkhoven RM, van Vliet MH, Wessels LF, and Peterse JL, et al (2007). Somatic loss of BRCA1 and p53 in mice induces mammary tumors with features of human *BRCA1*-mutated basal-like breast cancer. *Proc Natl Acad Sci U S A* **104**, 12111–12116.

[32] Rottenberg S, Nygren AOH, Pajic M, van Leeuwen FWB, van der Heijden I, van de Wetering K, Liu X, de Visser KE, Gilhuijs KG, and van Tellingen O, et al (2007). Selective induction of chemotherapy resistance of mammary tumors in a conditional mouse model for hereditary breast cancer. *Proc Natl Acad Sci U S A* **104**, 12117–12122.

[33] Inoue Y, Izawa K, Kiryu S, Tojo A, and Ohtomo K (2008). Diet and abdominal autofluorescence detected by *in vivo* fluorescence imaging of living mice. *Mol Imaging* **7**, 21–27.

[34] Nachabé R, Hendriks BH, Desjardins AE, van der Voort M, van der Mark MB, and Sterenborg HJ (2010). Estimation of lipid and water concentrations in scattering media with diffuse optical spectroscopy from 900 to 1,600 nm. *J Biomed Opt* **15**, 037015.

[35] Farrell TJ, Patterson MS, and Wilson B (1992). A diffusion theory model of spatially resolved, steady-state diffuse reflectance for the noninvasive determination of tissue optical properties *in vivo*. *Med Phys* **19**, 879–888.

[36] Zonios G and Dimou A (2009). Light scattering spectroscopy of human skin *in vivo*. *Opt Express* **17**, 1256–1267.

[37] Nachabé R, Hendriks BH, van der Voort M, Desjardins AE, and Sterenborg HJ (2010). Estimation of biological chromophores using diffuse optical spectroscopy: benefit of extending the UV–VIS wavelength range to include 1000 to 1600 nm. *Biomed Opt Express* **1**, 1432–1442.

[38] Müller M and Hendriks BH (2013). Recovering intrinsic fluorescence by Monte Carlo modeling. *J Biomed Opt* **18**, 27009.

[39] Müller MG, Georgakoudi I, Zhang Q, Wu J, and Feld MS (2001). Intrinsic fluorescence spectroscopy in turbid media: disentangling effects of scattering and absorption. *Appl Opt* **40**, 4633–4646.

[40] Zhang Q, Müller MG, Wu J, and Feld MS (2000). Turbidity-free fluorescence spectroscopy of biological tissue. *Opt Lett* **25**, 1451–1453.

[41] Ostrander JH, McMahon CM, Lem S, Millon SR, Brown JQ, Seewaldt VL, and Ramanujam N (2010). Optical redox ratio differentiates breast cancer cell lines based on estrogen receptor status. *Cancer Res* **70**, 4759–4766.

[42] Skala MC, Riching KM, Gendron-Fitzpatrick A, Eickhoff J, Eliceiri KW, White JG, and Ramanujam N (2007). *In vivo* multiphoton microscopy of NADH and FAD redox states, fluorescence lifetimes, and cellular morphology in precancerous epithelia. *Proc Natl Acad Sci U S A* **104**, 19494–19499.

[43] Sorg BS, Moeller BJ, Donovan O, Cao Y, and Dewhirst MW (2005). Hyperspectral imaging of hemoglobin saturation in tumor microvasculature and tumor hypoxia development. *J Biomed Opt* **10**, 44004.

[44] Teicher BA, Holden SA, Ara G, Dupuis NP, Liu F, Yuan J, Ikebe M, and Kakeji Y (1995). Influence of an anti-angiogenic treatment on 9L gliosarcoma: oxygenation and response to cytotoxic therapy. *Int J Cancer* **61**, 732–737.

[45] Croce AC, Santamaria G, De Simone U, Lucchini F, Freitas I, and Bottiroli G (2011). Naturally-occurring porphyrins in a spontaneous-tumour bearing mouse model. *Photochem Photobiol Sci* **10**, 1189–1195.

[46] Moesta KT, Ebert B, Handke T, Nolte D, Nowak C, Haensch WE, Pandey RK, Dougherty TJ, Rinneberg H, and Schlag PM (2001). Protoporphyrin IX occurs naturally in colorectal cancers and their metastases. *Cancer Res* **61**, 991.

[47] Brown JQ, Wilke LG, Geradts J, Kennedy SA, Palmer GM, and Ramanujam N (2009). Quantitative optical spectroscopy: a robust tool for direct measurement of breast cancer vascular oxygenation and total hemoglobin content *in vivo*. *Cancer Res* **69**, 2919–2926.

[48] Santos CR and Schulze A (2012). Lipid metabolism in cancer. *FEBS J* **279**, 2610–2623.

[49] Boren J and Brindle KM (2012). Apoptosis-induced mitochondrial dysfunction causes cytoplasmic lipid droplet formation. *Cell Death Differ* **19**, 1561–1570.

[50] Partridge SC, Gibbs JE, Lu Y, Esserman LJ, Tripathy D, Wolverton DS, Rugo HS, Hwang ES, Ca Ewing, and Hylton NM (2005). MRI measurements of breast tumor volume predict response to neoadjuvant chemotherapy and recurrence-free survival. *Am J Roentgenol* **184**, 1774–1781.

[51] Gerlinger M, Rowan AJ, Horswell S, Larkin J, Endesfelder D, Gronroos E, Martinez P, Matthews N, Stewart A, and Tarpey P, et al (2012). Intratumor heterogeneity and branched evolution revealed by multiregion sequencing. *N Engl J Med* **366**, 883–892.

[52] Nachabé R (2012). Diagnosis with near infrared spectroscopy during minimally invasive procedures. The Netherlands: Erasmus University Rotterdam; 2012. p. 201–210.